ANALYSIS OF SOLAR RECEIVER PERFORMANCE FOR CHEMICAL-LOOPING INTEGRATION WITH A CONCENTRATING SOLAR THERMAL SYSTEM

Zhiwen Ma[1]
National Renewable Energy Laboratory
15013 Denver West Parkway, Golden, CO 80401, USA
e-mail: zhiwen.ma@nrel.gov
ASME Membership (100134264)

Janna Martinek
National Renewable Energy Laboratory
15013 Denver West Parkway, Golden, CO 80401, USA
e-mail: Janna.Martinek@nrel.gov

ABSTRACT

This paper introduces a chemical-looping configuration integrated with a concentrating solar thermal (CST) system. The CST system uses an array of mirrors to focus sunlight, and the concentrated solar flux is applied to a solar receiver to collect and convert solar energy into thermal energy. The thermal energy then drives a thermal power cycle for electricity generation or provides an energy source to chemical processes for material or fuel production. Considerable interest in CST energy systems has been driven by power generation, with its capability to store thermal energy for continuous electricity supply or peak shaving. However, CST systems have other potential to convert solar energy into fuel or to support thermochemical processes. Thus, we introduce the concept of a chemical-looping configuration integrated with the CST system that has potential applications for

[1] Corresponding author

thermochemical energy storage or solar thermochemical hydrogen production. The chemical-looping configuration integrated with a CST system consists of the following: a solar-receiver reactor for solar-energy collection and conversion, thermochemical energy storage, a reverse reactor for energy release, and system circulation. We describe a high-temperature reactor receiver that is a key component in the chemical-looping system. We also show the solar-receiver design and its performance analyzed by solar-tracing and thermal-modeling methods for integration within a CST system.

Keywords: Concentrating solar thermal, chemical looping, solar thermochemical process, solid particles

INTRODUCTION

Solar thermochemical processes have been broadly explored in the area of metal-oxide reduction, solar thermochemical hydrogen (STCH) production, fuel processing (e.g., pyrolysis), and thermochemical energy storage (TCES) for a concentrating solar power (CSP) plant [1-9]. CST technologies include parabolic trough, linear Fresnel, power tower, and parabolic dish configurations with various solar-collector designs, energy-collection temperatures, and thermal efficiencies. CST power-tower systems are typically deployed as large, centralized power plants to take advantage of economies of scale and provide the platform that collects solar energy and converts it into thermal or thermochemical energy by implementing relevant processes for power or fuel production. The chemical media for TCES or STCH material are often metal oxides, with recent attention primarily focused on various perovskite materials. The metal oxides are reduced at high temperature, and then re-oxidized with either air (TCES) or steam (STCH) at comparatively lower temperature to complete the cycle.

Metal oxides or perovskite materials integrated with a CST power system using TCES offer the following advantages: 1) Chemical-energy storage can serve long-duration needs of days or weeks. The long energy-storage duration can overcome day-to-day variation of renewable generation to meet the grid demand through different time periods. 2) High-density and -quality energy can be stored and support high-performance thermal/power conversion cycles. When using TCES for power generation, the reduction and oxidation temperatures of the metal oxide may be selected relevant to the power-cycle temperature range. For example, TCES integrated with a steam-Rankine power cycle can be in the range from 200° to 750°C, and the temperature cycle of a TCES for a supercritical carbon dioxide (sCO_2) power cycle may be in the range from 500° to

900°C. The temperature range affects the receiver material selection, design, and thermal performance.

Metal oxides or perovskite materials can also be integrated with a CST system for hydrogen production through water splitting using a high-temperature STCH process. Hydrogen is often the first and foremost step in renewable fuel production through water splitting. Once the methods for hydrogen production from water splitting are economically available, the combination of carbon dioxide (CO_2) and synthesis into hydrocarbon fuel is a foreseeable next step [7]. For example, Fischer-Tropsch synthesis is an established industrial process using hydrogen to produce liquid hydrocarbon fuels that can be delivered by directly using the existing petroleum infrastructure [10]. An additional development pathway is to generate liquid methanol blended with petroleum as a renewable fuel component. Methanol can be produced by directly reacting solar-generated hydrogen and captured or recycled CO_2 via an established industrial process. Another promising pathway is combining solar hydrogen with nitrogen from air separation to yield ammonia—an easily liquefied chemical with known shipping and handling protocols [11, 12].

A solar thermochemical process can be built on a cycling loop in a chemical-looping configuration for energy conversion and storage [13], which can be a solar thermochemical platform when integrating with a receiver reactor as solar energy inputs. The chemical-looping concept and configuration extended into the CST system generalize the solar thermochemical cycle with the link between a process and a component. Each process represents a chemical-looping configuration, with solar energy providing the energy necessary for the high-temperature reduction reaction.

A chemical-looping CST system can be built on a power-tower system with an array of heliostats that concentrate solar flux onto a central receiver. A preferred arrangement for the

chemical reduction of metal oxide is to absorb the solar energy in a receiver reactor. However, the metal-oxide reduction temperature for ceria or similar materials is often high (>1,500°C), making it difficult to improve the efficiency of a thermochemical process [14]. Recent metal-oxide studies have focused more on perovskite materials [15]. The high temperatures needed by the chemical processes require a solar-receiver reactor able to operates at high temperatures with high thermal efficiency. The receiver is configured to transfer thermal energy from the sunlight to the chemical substance through a thermochemical process. Figure 1 depicts a CST system that uses the planar-cavity receiver for electricity generation. The chemical-looping configuration for TCES or STCH using metal-oxide particles can be built upon the particle-based CST platform as discussed in the last section of this paper. This paper focuses on a novel receiver configuration and initial performance analysis for a TCES application.

2. PLANAR-CAVITY RECEIVER DEVELOPMENT FOR HEATING HIGH-TEMPERATURE PARTICLES

A solar-receiver design affects the overall energy-conversion efficiency and is critical to the CST system performance. Many chemical reactions in solar thermochemical processes involve solid particles or gas phases at high temperatures (often >800°C). Although particle-based CST technology may support high operating temperatures in the range suitable for a solar thermochemical process, the major challenge is developing a solar receiver that can effectively capture the solar heat by the particulate materials with high efficiency. Current particle-receiver configurations include open-cavity falling-particle designs [16-20], open-cavity obstructed-flow designs [16, 21], enclosed falling-particle designs [22-24], rotating-cavity designs [25], and directly or indirectly irradiated fluidized-bed designs [26]. Open-cavity configurations theoretically provide a rapid particle-heating rate, but they expose the particulate material directly to ambient air; therefore, they do not permit control over the gas-phase environment that

is necessary to establish atmospheric conditions favorable for a metal-oxide reduction reaction. Furthermore, performance can be influenced by particle loss through the open aperture and by entrainment of cold ambient air within the particle curtain [16-19].

An enclosed-particle receiver can offer the chemical-reaction conditions needed for a solar thermochemical process and can reduce heat loss to the ambient environment at high temperatures. The heat transfer for all types of heat-transfer media (HTM) needs to be optimized for reducing the receiver surface temperatures to minimize thermal losses. Heat-transfer coefficients between walls and flowing solids are typically in the range of 100–700 $W/m^2 \cdot K$, which is insufficient to maintain manageable wall temperatures if exposed to the high aperture solar-flux concentrations (on the order of 1 MW/m^2). Because the high receiver wall temperatures incur large loss through convection and radiation to the environment, controlling the temperature differences between the HTM and the receiver panel walls is needed to achieve a high thermal efficiency. Thus, heat-flux spreading on the receiver wall is necessary to accommodate both high aperture flux concentration and comparatively low solids-phase heat-transfer capability involving gas or solid-particle media in solar-receiver design.

To achieve high thermal efficiency at an operating temperature above 800˚C with a controlled gas condition, we developed an enclosed receiver in which the flowing particles and are in contact with the panel walls heated by the solar flux, as shown in Figure 2. The particle receiver uses flat-panel cavity walls and, for the TCES application, is constructed from a high-temperature metal alloy that naturally oxidizes to form an absorptive surface. With proper design and alignment with the incoming solar beam, solar flux is spread along the cavity panels. The planar cavity shields the particle materials from the environment; therefore, the receiver is suitable for a thermochemical process that needs a reaction condition differing from the ambient environment and can

theoretically maintain a high temperature and efficiency. The planar cavity is formed by panel walls that can be fabricated from sheet metal or ceramic materials depending on the application temperatures, working conditions, and mechanical design. The leading edge of the panel may contain a heat shield containing liquid cooling to accept high solar flux at the receiver front aperture if the HTM is inadequate to cool the front edge. Options include a suitable high-temperature heat pipe or preheating liquid water.

Figure 2 shows the receiver design and the planar-cavity receiver module formed by the vertical panels. An array of such panels is arranged along the periphery of a cylindrical shape to form a large receiver assembly on top of a central tower. Particles flow inside the enclosed passages formed by the panels of the cavity walls. The particle flow can be in a moving-bed or fluidized-bed pattern. The particle/panel interaction is an important research subject to enhance the heat transfer from the cavity wall to particles. The enclosed flow passage formed by the panels not only minimizes the direct particle heat loss to the ambient but also provides the atmospheric condition benefiting the thermochemical process. As shown in Figure 2, panels can be tapered to spread the concentrated solar flux on the side walls, where the distributed heat flux can be managed by matching the wall-to-particle heat-transfer capability.

The enclosed receiver for reducing metal-oxide particles can be held under vacuum to remove oxygen or can use an inert purge gas to increase the reduction conversion for metal oxide. The receiver design has good scalability from a small-scale prototype verification to a full-scale commercial receiver. The fabrication of the panel walls depends on panel materials that are selected by application temperatures and HTM. A planar-cavity receiver design using perovskite material ($CaCr_{0.1}Mn_{0.9}O_{3-\delta}$) for thermochemical energy storage was designed for testing reduction

reaction at about 900°C [27]. Inconel-alloy sheet metal was used in the receiver design and we target 1,050°C as the upper limit of the receiver-panel temperatures.

3. SOLAR-RECEIVER PERFORMANCE MODELING

The solar flux incident on the cavity aperture of the central-tower receiver originates from a surrounding heliostat field. The interaction between the solar flux and the receiver panels depends on the solar-field layout and solar aiming strategy, as well as on location, date, and time of day. Here, we consider only a single set of design-point conditions. Our receiver performance model considers: 1) local solar-flux absorption from the surrounding heliostat field, 2) solid-particle heat transfer with the panel walls, and 3) computational fluid dynamics (CFD) simulation of air flow surrounding the heated receiver and heat losses induced by natural convection and infrared radiative exchange between the heated walls and surrounding environment. The solar flux and CFD modeling method and the results are discussed in the following sections.

3.1 Solar-Receiver Geometry and Model Setup

Solar-flux absorption is simulated using the Monte Carlo ray-tracing method within the SolTrace software developed by the National Renewable Energy Laboratory (NREL). The solar field was set up as a surround field, and a cylindrical receiver with multiple planar cavities was positioned on top of a central tower. The objectives of modeling efforts for the full-scale receiver are to select appropriate receiver dimensions, shape, and operating conditions, and to characterize the thermal performance including the heat-pipe heat shield. We select panel sizing/orientation to maintain a low local wall-absorbed flux (<200 kW/m^2) despite high surface absorptivity (0.9) and high incident aperture flux (≥1,000 kW/m^2). Relevant performance metrics include peak wall temperatures, solids temperature evolution over the full 16-m receiver height, and full-scale receiver thermal efficiency. Performance targets include a peak receiver-wall temperature within

the panel material limit with an aperture flux of ≥1,000 kW/m^2. The full-scale receiver consists of individual cavities (schematically illustrated in Figure 2) positioned around the circumference of a cylindrical receiver.

The receiver design employs a method for high solar flux to be spread along the cavity walls to reduce the local absorbed heat-flux concentration to a level well below the aperture flux concentrations. Thus, the wall heat flux can be absorbed by HTM with low heat-transfer capabilities such as solid particles or gases with a manageable temperature difference between the HTM and the receiver walls. Because the flux spreading is accomplished purely by cavity sizing and geometric alignment of the cavity walls relative to the incoming beams, the performance of a given receiver configuration is highly dependent on the directional nature of the incoming beams. A full analysis of interactions between heliostat-field design choices, aiming algorithms, and the selected size/shape and performance of the receiver cavity is a multi-factor optimization problem. This paper focuses primarily on demonstrating the flux simulation methods and the effect of flux spreading on the cavity panel walls. The flux-distribution results have not been optimized for all design parameters. Figure 3 shows the cavity sizing parameters. The leading edge of the receiver panel is subject to high incident solar flux, and it may not be adequately cooled by the particles or gas phase. One solution for accommodating high heat flux on the leading edge is to use a heat pipe as a heat shield to spread the heat flux inside the panel chamber for heat transfer with particles or gases, as illustrated in Figure 3.

3.2 Solar-Flux Characterization for the Planar-Cavity Design

The flux modeling used a heliostat field and tower height that were imported directly into the SolTrace program from SolarPILOT simulation results. Figure 4a shows a solar-field layout designed for a receiver thermal capacity (500 MW_{th}) and targeted peak aperture flux magnitude (1

MW/m^2) on the north-facing cavity aperture positioned on a 15-m-diameter and 16-m-tall receiver cylinder. The field consists of 6,895 144m^2 heliostats , a tower height of 150 m, assumed to be located in Daggett, CA. The solar-field simulation used the SolarPILOT software package developed at NREL [28] and selected a single heliostat-field layout and aiming strategy. After the solar-field layout was obtained from SolarPILOT, the flux distributions on the cavity walls were obtained from ray-tracing simulations with light rays originating from the sun and traced through the optical system. The heliostat layout coordinate locations and aim points, surface optical properties, and geometry of the tower and receiver cavities were set up in the SolTrace model for ray-tracing analysis. The model simulates absorbed solar flux profiles on the planar-cavity wall panels at the design point. The surface optical properties include reflectivity, transmissivity, slope error, and specularity error. The heliostats were simulated with a reflectivity of 0.93, slope error of 1.53 mrad, and specularity error of 0.2 mrad. The panel reflectivity in the solar spectrum is based on the hemispherical reflectivity at the near-normal incidence of an oxidized Haynes 230 sample, which was experimentally measured at NREL to be approximately 0.1 and was assumed to reflect diffusely. At each interaction, SolTrace first determines if the ray will be absorbed, reflected, or transmitted based on the optical properties of the element it contacted. If it is not absorbed, then the resulting reflected ray will be determined by the optical properties, the geometry of the element, and incident direction relative to the element surface normal. Solar flux that is not absorbed by any element of the receiver is reflected back to the environment and the reflective loss, η_{ref}, is expressed as:

$$\eta_{ref} = 1 - \frac{Q_{aborbed}}{Q_{sol,inc}} \quad (1)$$

Where $Q_{sol,inc}$, is the solar flux incident on the receiver aperture area. The SolTrace simulation utilized 10^9 rays per simulation and provides both the reflective loss described above and the solar absorption profiles along the planar cavity receiver walls.

A baseline study was conducted for one of the cavities facing the north. The resulting flux profile on a single 16.4-cm x 16-m north-facing planar-cavity aperture at design point is shown in Figure 4b. Predicted peak aperture flux is less than 1,100 kW/m^2, with an average aperture flux of 960 kW/m^2. South, east, and west-facing cavities receive less solar energy and a lower peak flux under design point conditions. Thus, we constrain our initial analysis to the north-facing cavity that receives the highest design point flux concentration and thus reaches the highest peak temperatures. The low-flux regions at the top and bottom of the aperture result from the heliostat aiming strategy, which ensures that the heliostats provide the necessary flux on the desired aperture with a focus on collecting flux near the aperture center and thereby reducing spillage for less than 2% by the SolarPILOT model. Given the heliostat layout and resulting aperture flux profile depicted in Figure 4, this study aims to evaluate the sensitivity of receiver solar-absorption performance relative to cavity design and to select an initial panel configuration for further thermal analysis. The receiver geometry is parameterized as indicated in Figure 3. In each receiver configuration, each of the back two panels (thick green and thick black lines in Figure 3) contains the reactive particles directly behind the panel wall. To maintain a suitable temperature difference between the particles and the panel wall, the solar energy absorbed on these walls must be limited to values that match the expected particle/wall heat-transfer capability.

Cavity sizing parameters were selected based on absorbed flux profiles from ray-tracing simulations. The parameterized receiver configuration offers a large number of degrees of freedom that can be tuned to ensure acceptable absorbed flux concentrations. The analysis and results

reported below have only explored a limited subset of the parameter space to provide design directions for manifesting the flux profile control. All calculations described below assume that the absorptivity of each of the panels and the heat shield is 90% and that surfaces reflect with a specularity error of 1,500 mrad. This large specularity error was used to approximately represent diffuse reflection behavior. Parameters are held constant in the results reported in this section are: $D_1 = 0.076\ m$, $D_2 = 0.127\ m$, $\theta_1 = 30°$, $W_1 = 0.088\ m$. The sensitivity studies of the cavity dimensions were primarily on varying θ_2, θ_3, and W_1. Figures 5 and 6 illustrate the sensitivity of peak absorbed panel flux to the front-cavity aperture width and panel size and orientation. Simulations in Figure 5 maintain fixed $D_3 = 0.127\ m$ while adjusting the back width of the cavity (W_2) via alteration of the middle panel angle θ_2. In addition to the results shown in Figure 5, peak flux values on the middle panel (Panel 2, green lines in Figure 3) were found to be only weakly sensitive to D_3 and varied by at most 5% as D_3 increased from 0.127 m to 0.1778 m. This is to be expected given the high absorptivity of each panel. Values of $\theta_2 < 0$ in Figure 5 imply that Panel 2 is angled opposite the direction illustrated in Figure 3, thereby creating a slightly concave particle channel. This negative angle serves to better align Panel 2 with rays that enter the aperture with a large azimuth angle relative to the aperture normal and appears necessary to maintain low peak flux on Panel 2. Results in Figures 6 and 7 were obtained by simultaneously varying W_2 and D_3 with W_1 fixed at either 0.0762 m (3in, solid lines) or 0.0635 m (2.5in, dashed lines) and they illustrate Panel 3 average and peak flux, respectively. Peak and average absorbed fluxes decrease as both the overall cavity width decreases and the back-vertex angle narrows.

A tentative initial target for solar-flux absorption was desirable in the range of 100–150 kW/m^2, which would be expected to produce an approximate 200-300°C wall-to-particle temperature difference based on an assumed total particle heat-transfer coefficient of 500 W/m^2·K, including

both convection and radiation heat transfer. The smallest overall predicted peak absorbed flux for the region of design space explored to date is still somewhat above the original target of 100–150 kW/m^2. However, the parameter sensitivity described by Figures 5 and 6 provides direction for continued analysis of the receiver configuration and offers an indication that the proposed receiver configuration can be optimized for the desired performance in a realistic full-scale surround-field configuration. The north-facing cavity examined within this study is expected to receive the most energy and, correspondingly, is the worst-case cavity regarding peak flux magnitude. Based on the planar-cavity design principals presented in the paper, design-parameter variations can be optimized for various design needs according to the HTM heat-transfer capability and operating conditions, including deeper cavities, $\theta_2 < 0$ (concave design), and analysis of parameters (D_1, D_2, θ_1) that were held constant in this initial screening study.

3.3 CFD Modeling of the Solar-Receiver Performance

Receiver temperature profiles, natural convective effect, infrared radiative exchange, and particle heat-transfer resistance are all simulated in a 3-D CFD model using ANSYS-Fluent software. The north-facing cavity of the full 16-m-tall receiver module is selected because it is anticipated to receive the highest concentration of solar energy; thus, it is subjected to the highest wall temperatures.

The standard conservation equations (conservation of mass, momentum, and energy) for the surrounding ambient environment were solved to obtain the natural convection and radiative losses of the receiver. The size and operating temperature of the solar receiver can induce turbulent natural convection conditions without the influence of the wind flow. Turbulent flow can be approximated by the Reynolds-Averaged Navier-Stokes (*RANS*) Equations in (2) and (3):

$$\nabla \cdot \left(\rho \vec{V}\right) = 0 \tag{2}$$

$$\nabla \cdot \left(\rho \vec{V} \vec{V}\right) = -\nabla p + \rho \vec{g} + \nabla \cdot (\vec{\bar{\tau}} - \rho \overline{\vec{V}' \vec{V}'}) \tag{3}$$

where the viscous stresses are given by:

$$\vec{\bar{\tau}} = \mu \left[\left(\nabla \vec{V}\right) + \left(\nabla \vec{V}\right)^T\right] + \frac{2}{3}\left(\nabla \cdot \vec{V}\right)\vec{\bar{I}} \tag{4}$$

Closure equations are required to represent the Reynolds stress terms, $-\rho \overline{\vec{V}' \vec{V}'}$, which can be approximately related to the time-averaged fluid velocity via the Boussinesq hypothesis. The *k*-ω shear-stress transport (SST) turbulence model in ANSYS-Fluent was used for modeling the solar receiver because it has been shown to perform well in each wall-bounded, low-moderate Reynolds number, and far-field regime. Convective and conductive heat transfer is described by the energy equation given in Equation (5).

$$\nabla \cdot \vec{V}(\rho E + p) = \nabla \cdot (k \nabla T) \tag{5}$$

CFD simulations included only the solar-facing side of the planar-cavity receiver and surrounding ambient air that is optically non-participating. The size of the simulated external domain was selected by extending the position of the external boundaries until the point where an additional increase in external domain size did not alter the solution in the vicinity of the receiver. Exchange of radiative energy between the opaque walls can be approximately described by a surface-exchange model [29], where view factors are assessed on an element-to-element basis for each pair of CFD mesh elements. CFD results provide thermal losses of the receiver by natural

convection ($Q_{conv.loss}$) and thermal radiation ($Q_{rad.loss}$). Then the receiver efficiency, $\eta_{receiver}$, can be obtained from the calculated losses:

$$\eta_{thermal} = \frac{Q_{absorbed} - Q_{conv.loss} - Q_{rad.loss}}{Q_{sol,inc}} \quad (6)$$

The panel walls heated by incident solar-flux heat solid particles by convective, conductive, and radiative heat transfer. In this initial analysis, we do not fully simulate the full complexity of hydrodynamics and heat transfer behavior of the dense-phase particle flow behind the receiver panels. Rather, the rate of heat transfer is defined by a local solids temperature and heat-transfer coefficient consisting of a fixed convective/conductive component and a temperature-dependent radiative component. For the gas/particle two-phase flow within the receiver reactor, we used a similar approach employed by [30] for bubbling fluidized beds, which is the gas/particle flow regime of the perovskite TCES in the CST power system. The effective radiative heat-transfer coefficient is defined in Equation (7):

$$h_{rad} = \frac{\sigma\left(T_w^2 + T_s^2\right)\left(T_w + T_s\right)}{1 + \left(1 - \varepsilon_w\right)/\varepsilon_w + \left(1 - \varepsilon_{bed}\right)/\varepsilon_{bed}} \quad (7)$$

The radiative contribution is evaluated locally from the temperature of each wall-surface mesh element via a user-defined subroutine inside the CFD software and combined with the fixed convective/conductive component to produce the total wall-to-solids local heat-transfer coefficient. The multiphase flow behind the panels is not directly simulated; however, two-way coupling between wall and solids temperatures is achieved by allowing the solids temperature to evolve along the receiver height from the top (inlet) to the bottom (outlet) by means of a simple steady state one-dimensional energy balance. This energy balance is implemented as a user-defined subroutine and calculates the solids temperature as a function of height based on the solids mass flow rate, heat capacity, and a position-dependent heat input derived from the heat-transfer

rates at all wall mesh elements in contact with the particle-flow channel at each height position. The solids mass flow was iteratively adjusted during the CFD model solution to achieve the desired solids outlet temperature. Simulations incorporate the spatial profile of absorbed solar flux as a boundary condition and include a meshed panel wall. The sodium-vapor heat pipe on the leading edge is simulated using a solid body with constant, high effective thermal conductivity. Heat pipes spread the heat from the leading edge along their walls and heat the particles inside the particle flow chamber as shown in Figure 3. A high-temperature heat pipe can absorb high thermal flux in its evaporation chamber to absorb the high solar flux on the front edge and to spread heat inside the particle enclosure for heat transfer to particles inside. A sodium-vapor heat pipe can be a candidate heat shield with its constant, high effective thermal conductivity. Although the value of the thermal conductivity is not known precisely, manufacturer information suggests that an effective thermal conductivity exceeding 5,000 W/m·K is achievable in a working temperature range of 500°–1,100°C [31].

Table 1 provides base cavity sizing and simulation parameters. The sizing parameters in Table 1 were selected for low peak absorbed flux given potential constraints on minimum solids channel sizing. The two configurations in Table 1differ only in the heat-shield vertex angle such that one configuration ($\theta_1 = 25°$) has a larger cavity aperture and solids channel width, and the second configuration ($\theta_1 = 20°$) has a smaller cavity aperture and solids channel width. Angle θ_1 directly affects with the solar-flux interception and reflection from the half solar field facing the cavity, and meanwhile, it affects the external convection and infrared radiation to the environment. Geometry 1 has a θ_1 angle of 25°, and Geometry 2 has a θ_1 angle of 20°. Absorbed flux profiles and temperature profiles are illustrated in Figures 8.a and 8.b for Geometry 1. Figure 8 illustrates

the simulated wall temperature distribution for the north-facing cavity with solids inlet/outlet temperatures of 500°C/900°C.

Figure 9 shows the temperature profiles in the cavity walls and surrounding ambient environment with base-case input parameters at the midpoint of the cavity height and 1 m above the bottom of the receiver cavity. The cold temperature in front of the cavity and the hot temperature on the cavity back show the effect of the thermal shield by the cavity design.

The results of flux absorption are summarized in Table 2 along with results from the thermal-performance CFD simulations with base parameters in Table 1. Table 2 describes the simulated solar-flux distribution and thermal performance for two configurations with solids inlet/outlet temperatures of 500°C/900°C and 200°C/750°C. Peak wall-absorbed solar flux is 220–235 kW/m^2, with a north-facing cavity average aperture flux of 1,055 kW/m^2. Peak simulated panel-wall temperatures are about 1,080°C for the high-solids temperature conditions and 965°C for the comparatively lower-solids temperature conditions. North-facing cavity thermal efficiency ($\eta_{thermal}$) is defined as the energy transferred into the solids phase divided by the energy incident on the aperture of the cavity and is predicted to range from 82.6% for the high-solids temperature conditions to 88.4% for the lower-solids temperature conditions.

In addition to the reactive-material inlet/outlet temperatures (500°C/900°C) used in this analysis, calculations with typical inlet/outlet conditions for an inert solids receiver (200°C/750°C) are included for comparison. Peak wall temperature for the high-temperature conditions in Table 1 is 1,087°C. However, because peak wall temperatures are strongly tied to local flux absorption, additional improvements in flux-absorption uniformity may enable further wall-temperature reduction. Furthermore, empirical correlations and multiphase simulations of fluidized beds

typically indicate an increase in the convective heat-transfer coefficient with surface temperature due to an increase in gas thermal conductivity and a corresponding reduction in gas-film thermal resistance with temperature. Although the temperature-dependent radiative heat-transfer contribution was included in the current study, temperature variability of the convective component was neglected given overall uncertainty in the heat-transfer coefficient. The overall heat-transfer coefficient of 500 $W/m^2 \cdot K$ may be overly conservative within the hottest temperature regions of the receiver.

Figure 10 illustrates the sensitivity of north cavity-wall temperatures and efficiency to the solids-wall convective heat-transfer coefficient—a parameter that is critical to receiver thermal performance but is highly uncertain currently. An increase in the convective component of the solids-wall heat-transfer coefficient to 500 $W/m^2 \cdot K$ would reduce the peak wall temperature to 1,035°C. The narrow but high-temperature operating condition for the solar receiver incurs thermal emission with a fourth-power dependence on temperature. The reduction in thermal efficiency when moving from traditional CSP operating conditions to the higher-temperature reactive operating conditions can be primarily attributed to additional thermal radiation losses. However, achieving 90%, thermal efficiency would be challenging at the high-temperature operating conditions even with highly effective solids-wall heat-transfer rates. Conversely, lower-temperature inert-material operating conditions (200°C inlet, 750°C outlet) can maintain wall temperatures below 1,050°C and may approach 90% thermal efficiency if the heat transfer on the particle side is adequate (e.g., >500 $W/m^2 \cdot K$).

Flux-distribution improvements to avoid excessively high surface temperatures could be investigated in future work to improve receiver performance. Also, the application of rigorous optimization techniques to receiver sizing, heliostat-field layout, and aiming strategies to

simultaneously optimize the flux distribution and thermal performance of the receiver would be beneficial. Although numerous cavity configurations were considered in this feasibility study, these did not include a variation of all possible design parameters, and they used only a single heliostat-field layout. Knowledge gained from future development can enhance certainty in sizing constraints (e.g., minimum solids channel size) to enable a meaningful optimization study. Nonuniform geometric sizing at different regions of the receiver (i.e., north-facing vs. south-facing) could also be considered. Applying highly absorptive or spectrally selective optical coatings on the leading-edge surfaces of heat pipes can improve solar absorption efficiency and possibly decrease thermal emissive loss.

4. INTEGRATING THE SOLAR-RECEIVER REACTOR WITH A CST CHEMICAL-LOOPING SYSTEM

The enclosed planar-cavity configuration is suitable for thermochemical processes that need a high-temperature and high-performance solar receiver with a controlled atmospheric condition. The receiver can be integrated within a chemical-looping system to enable the incorporation of solar energy as a heat source and provide a platform for solar energy collection, storage, power generation, or other thermochemical processes. Taking a generic metal-oxide material as an example for a solar thermochemical process, a chemical-looping cycle can utilize the high-temperature reduction (Equation 8) of the metal oxide in the solar receiver followed by a lower-temperature re-oxidation with either oxygen for thermochemical storage and power generation (Equation 9), or with steam for solar thermochemical hydrogen production (Equation 10).

$$Me_xO_y(s) \rightarrow Me_xO_{y-\delta}(s) + \delta/2\ O_2(g) \quad (8)$$

$$Me_xO_{y-\delta}(s) + \delta/2\ O_2(g) \rightarrow Me_xO_y(s) \quad (9)$$

$$Me_xO_{y-\delta}(s) + \delta\ H_2O(g) \rightarrow Me_xO_y(s) + H_2(g) \quad (10)$$

In the preceding analysis we focused on receiver design and performance for the application of thermochemical storage with a high particle temperature of up to 900°C. For the thermochemical storage application, reduced metal oxide from thermochemical storage is delivered to a fluidized-bed (FB) heat exchanger as needed [32]. Additionally, oxygen (O_2) gas can be delivered to the FB heat exchanger via a gas compressor to react with the reduced metal oxide in fluidization, releasing stored energy as heat. In an open-loop system, the oxygen gas is not stored and oxygen from ambient air is used as needed for the oxidation reaction. The heat that results from the oxidation reaction is transferred to a working fluid, such as water or sCO_2, in a heat exchanger to drive a power cycle. The chemical-looping system with metal-oxide particles for power generation incorporates major components in the particle-based CST platform as shown in Figure 1, including a particle receiver, thermochemical energy storage, and a particle-based heat exchanger.

The CST chemical-looping platform for the STCH process is necessarily different from the CST power system illustrated in Figure 1; however, the commonality between the two processes is the necessity of a high-temperature, high-efficiency receiver for the reduction reaction. The STCH reduction process occurs only when solar radiation is available. In such a case, the STCH system only works at on-sun condition, and may not store reduced particles, thus eliminating the energy storage subsystem. STCH processes have differing requirements for the reactive material and applicable materials typically require an increase in reduction temperature to >1,200°C. While the general receiver geometric configuration can theoretically promote high efficiency at high temperature, significant changes in receiver panel material and fabrication methods are required to support the >1,200°C temperature range required for STCH processes.

Conclusions

The planar-cavity receiver configuration consists of an array of panel receiver modules, which can be configured to control the solar-flux distribution absorbed on the receiver panel walls. The cavity configuration shields the high-temperature heat-transfer panels from the ambient environment for high thermal performance. The cavity receiver introduced in this paper is subject to high aperture solar-flux concentrations but spreads solar flux along the receiver walls to: (1) accommodate the lower heat-transfer capabilities of solid particles or gases, (2) reduce the temperature difference between the receiver walls and the HTM, and (3) reduce peak wall temperatures and thermal loss. The enclosed nature of the cavity receiver design can support high-temperature operation with high performance for thermochemical applications requiring a low-oxygen ambient environment.

The performance of an enclosed particle receiver was simulated for operating conditions between 200°C and 750°C (for thermal storage) or 500°C and 900°C (for thermochemical storage) and was predicted to achieve 88% or 83% thermal efficiency, respectively, for the north-facing cavity under design point conditions. The modeling outcomes provide a pathway to achieve high thermal efficiency. Further efforts can be devoted to optimizing the cavity design and assessing the performance of the whole planar-cavity receiver module including all cavity positions along the cylindrical receiver.

A particle-based CST system with enclosed particle receiver can support a thermochemical system using metal-oxide types of solid particles in a chemical looping configuration. The chemical-looping configuration integrated with a CST system can be a platform to accommodate solar-heat conversion to thermochemical energy through a chemical agent.

Acknowledgment

This work was authored by the National Renewable Energy Laboratory, operated by Alliance for Sustainable Energy, LLC, for the U.S. Department of Energy (DOE) under Contract No. DE-AC36-08GO28308. Funding provided by U.S. Department of Energy Office of Energy Efficiency and Renewable Energy Solar Energy Technologies Office. We are thankful for the SolTrace model developed by Tim Wendelin of NREL and the solar-flux work by Philip Hoskinson from San Diego State University. The authors acknowledge the funding support from the U.S. DOE through the ELEMENTS program for developing the mathematical model. We also acknowledge funding support from the DOE Fuel Cell Technology Office under the HydroGEN Program for preparing the manuscript.

References

1. Steinfeld, A., *Solar hydrogen production via a two-step water-splitting thermochemical cycle based on Zn/ZnO redox reactions.* International Journal of Hydrogen Energy, 2002. **27**: p. 9.
2. Lorentzou, S., et al., *Thermochemical CO2 and CO2/H2O splitting over NiFe2O4 for solar fuels synthesis.* Energy Procedia, 2013. **49**: p. 10.
3. Gokon, N., et al., *New Solar Water-Splitting Reactor with Ferrite Particles in an Internally Circulating Fluidized Bed.* Journal of Solar Energy Engineering, 2009. **131**: p. 9.
4. Kolb, G.J., R.B. Diver, and N. Siegel, *Central-Station Solar Hydrogen Power Plant.* Journal of Solar Energy Engineering, 2007. **129**: p. 5.
5. Hatamachi, T., T. Kodama, and Y. Isobe, *Carbonate Composite Catalyst with High-Temperature Thermal Sotrage for Use in Solar Tubular Reformers.* ASME, 2005. **127**: p. 5.

6. Ishihara, H., et al., *Two-Step Water Splitting Process With Solid Solution of YSZ and Ni-Ferrite for Solar Hydrogen Production.* Journal of Solar Energy Engineering, 2008. **130**: p. 3.
7. Perkins, C.M., et al., *Synthetic Gas Production by Rapid Solar Thermal Gasification of Corn Stover*, in *14th Biennial CSP SolarPACES Symposium*. 2008: Las Vegas, Nevada.
8. Rao, C.N.R. and S. Dey, *Generation of H2 and CO by solar thermochemical splitting of H2O and CO2 by employing metal oxides.* Journal of Solid State Chemistry, 2016. **242**: p. 9.
9. Steinfeld, A., *Solar thermochemical production of hydrogen—a review.* Solar Energy, 2005. **78**(5): p. 603-615.
10. Yali Yao, X.L., Diane Hildebrandt, David Glasser, *Fischer-Tropsch Synthesis Using H2/CO/CO2 Syngas Mixtures over an Iron Catalyst.* Industrial & Engineering Chemistry Research, 2011. **50**: p. 11.
11. T-Raissi, A., et al., *Hydrogen From Solar Via Light-Assisted High Temperature Water Splitting Cycles.* Journal of Solar Energy Engineering, 2007. **129**: p. 6.
12. Davidson, F.T., K. Nagasawa, and M.E. Webber, *Electro fuels - One way to store excess renewable electricity is to convert it to hydrogen, methane, or ammonia.* Mechanical Engineering, 2017. **139**(9).
13. Ma, Z., *Chemical Looping Fluidized-Bed Concentrating Solar Power System and Method, USPTO Patent Number 9,702,348 B2*. 2017.
14. Furler, P., et al., *Solar thermochemical H2O and CO2 Splitting utilizing a reticulated porous ceria redox system*. 2013: SUPSI. p. 14.
15. McDaniel, A. and I. Ermanoski, *High Efficiency Solar Thermochemical Reactor for Hydrogen Production*. 2017: DOE Annual Merit Review Project ID: PD113.
16. Ho, C.K., *A review of high-temperature particle receivers for concentrating solar power.* Applied Thermal Engineering, 2016.
17. Kim, K., et al., *A study of solid particle flow characterization in solar particle receiver.* Solar Energy, 2009. **83**(10): p. 1784-1793.
18. Siegel, N.P., et al., *Development and Evaluation of a Prototype Solid Particle Receiver: On-Sun Testing and Model Validation.* Journal of Solar Energy Engineering-Transactions of the Asme, 2010. **132**(2).
19. Tan, T., et al., *Wind effect on the performance of solid particle solar receivers with and without the protection of an aerowindow.* Solar Energy, 2009. **83**(10): p. 1815-1827.
20. Gobereit, B., et al., *Assessment of a falling solid particle receiver with numerical simulation.* Solar Energy, 2015. **115**: p. 505-517.
21. Lee, T., et al., *Numerical simulation of particulate flow in interconnected porous media for central particle-heating receiver applications.* Solar Energy, 2015. **113**: p. 14-24.
22. Ma, Z., et al. *Development of a Concentrating Solar Power System Using Fluidized-bed Technology for Thermal Energy Conversion and Solid Particles for Thermal Energy Storage*. in *Energy Procedia*. 2015.
23. Martinek, J. and Z. Ma, *Granular flow and heat-transfer study in a near-blackbody enclosed particle receiver.* Journal of Solar Energy Engineering, Transactions of the ASME, 2015. **137**(5).
24. Martinek, J., T. Wendelin, and Z. Ma, *Predictive performance modeling framework for a novel enclosed particle receiver configuration and application for thermochemical energy storage.* Solar Energy 2018. **166**: p. 409-421.
25. Wu, W., et al., *Prototype testing of a centrifugal particle receiver for high-temperature concentrating solar applications.* Journal of Solar Energy Engineering, Transactions of the ASME, 2015. **137**(4).
26. Flamant, G., et al., *Dense suspension of solid particles as a new heat transfer fluid for concentrated solar thermal plants: On-sun proof of concept.* Chemical Engineering Science, 2013. **102**: p. 567-576.
27. Ma, Z., *High-Temperature Thermochemical Storage with Redox-Stable Perovskites for Concentrating Solar Power, CRADA Number: CRD-14-554, NREL/TP-5500-70024*. 2017.
28. Wagner, M., *SolarPILOT program, https://www.nrel.gov/csp/solarpilot.html*.
29. Siegel, R. and J. Howell, *Thermal Radiation Heat Transfer, 4th edition*. 2002, New York: Taylor and Francis.
30. Chen, J.C., J.R. Grace, and M.R. Golriz, *Heat transfer in fluidized beds: design methods.* Powder Technology, 2005. **150**(2): p. 123-132.
31. Thermacore, *Heat Pipe Technology*. www.thermacore.com/thermal-basics/heat-pipe-technology.aspx.
32. Kunii, D. and O. Levenspiel, *Fluidization Engineering*. 2nd ed. 1991, Boston, MA: Butterworth-Heinemann.

NOMENCLATURE

D	planar-cavity depth (m)
E	internal energy of fluid (J/kg/K)
k	thermal conductivity (W/m/K)
h_{rad}	wall-to-particle radiative heat transfer coefficient (W/m^2/K)
p	pressure
$q''_{ap,solar}$	solar energy flux incident on cavity aperture (W/m^2)
Q_{absorb}	panel energy absorbed (W)
$Q_{conv,loss}$	natural convection loss (W)
$Q_{rad,loss}$	thermal emission loss (W)
$Q_{sol,inc}$	total solar energy incident on the cavity aperture (W)
T	temperature (K)
$\vec{V}$	velocity (m/s)
W	Planar-cavity aperture width (m)
δ	solids oxygen vacancy
ε_{bed}	effective solids bed emissivity
ε_{eff}	effective panel emissivity
μ	fluid viscosity (kg/m/s)
ρ	density (kg/m^3)
$\eta_{thermal}$	thermal efficiency of the planar-cavity receiver
θ	cavity panel angle
$\vec{\vec{\tau}}$	viscous stress tensor (kg/m/s^2)
Subscripts	
1, 2, 3	planar cavity panel number
s	solids
w	panel wall

Abbreviations

CFD	computational fluid dynamics

CST	concentrating solar thermal
HTF	heat-transfer fluid
TCES	thermochemical energy storage

Figure Captions List

Table Caption List

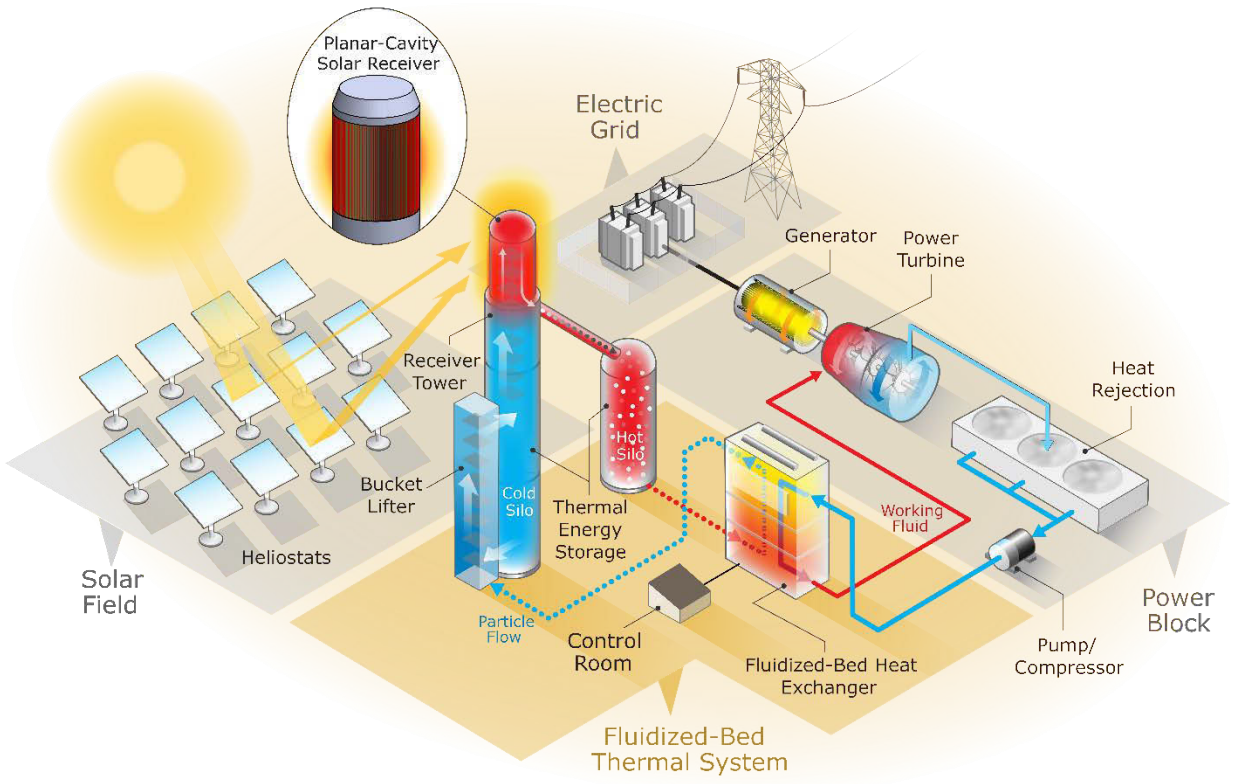

Figure 1. Particle-based CST platform for chemical-looping system using metal-oxide particles (Source: NREL).

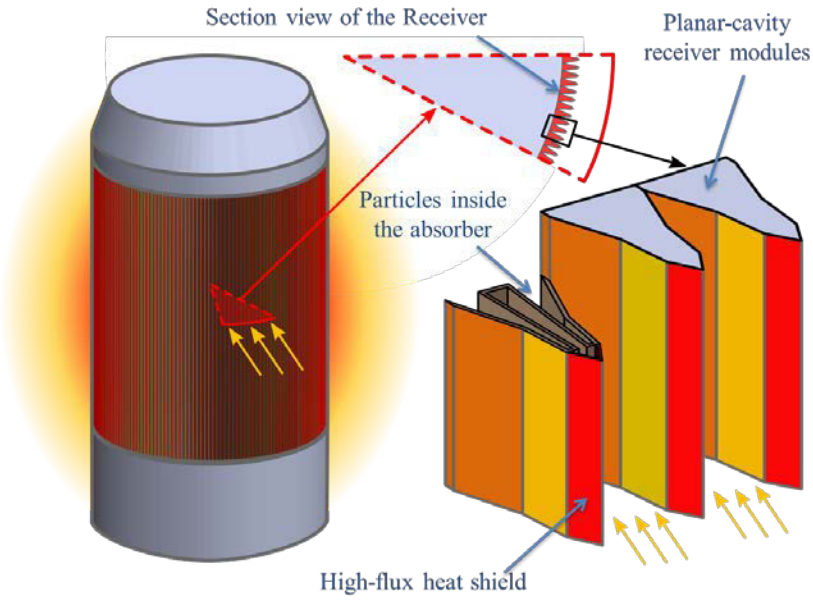

Figure 2. High-efficiency planar-cavity receiver design for high-temperature thermochemical process (Source: NREL).

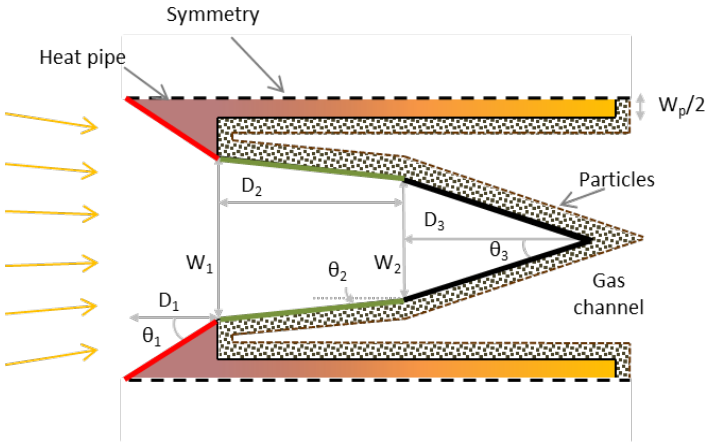

Figure 3. Top-view schematic of the full-scale receiver configuration including heat-pipe heat shield (Source: NREL).

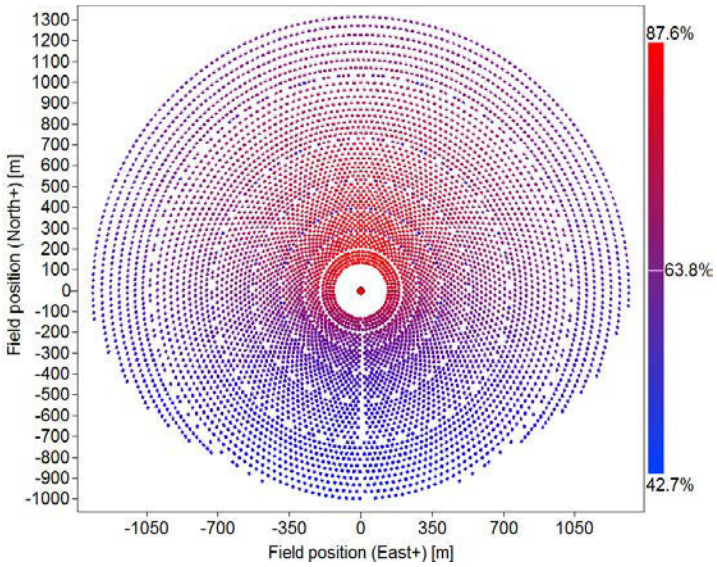

a. Heliostat-field layout and optical-efficiency profile

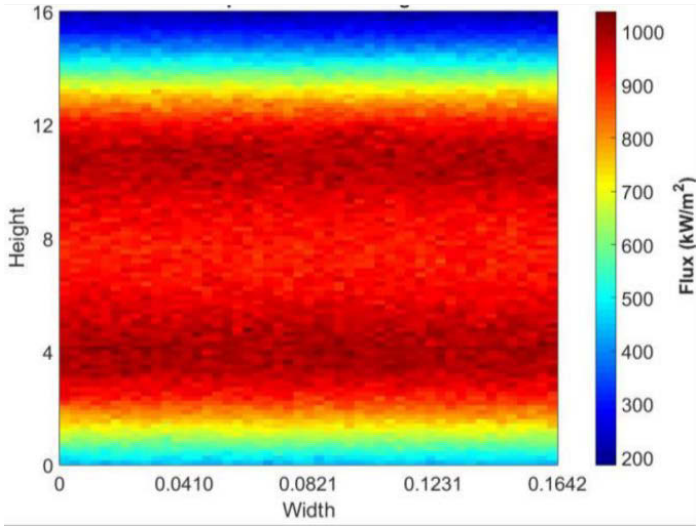

b. Aperture flux

Figure 4. Representative heliostat-field layout and the aperture flux distribution of one north-facing planar cavity.

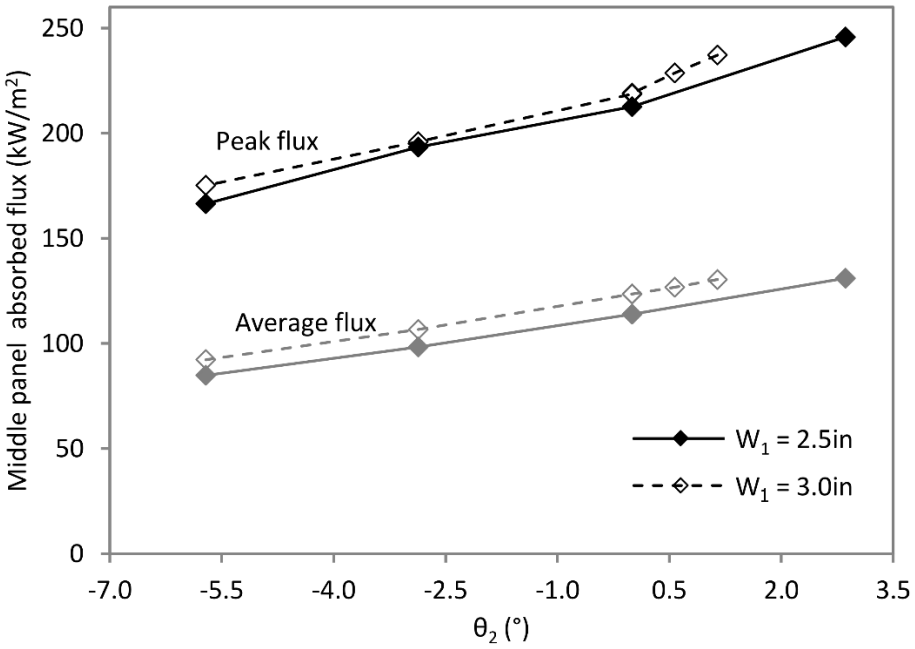

Figure 5. Sensitivity of middle panel (Panel 2) peak and average flux to W_1 and θ_2.

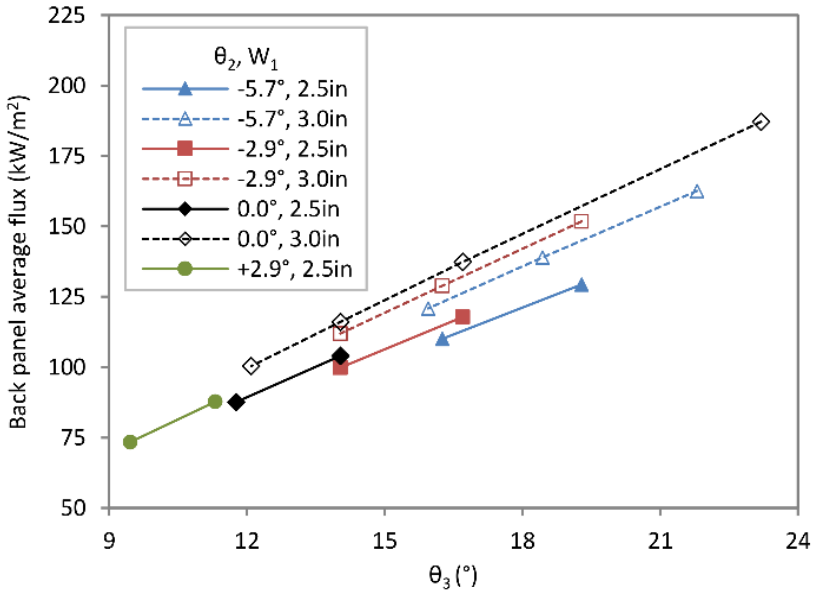

Figure 6. Back-panel (Panel 3) average flux.

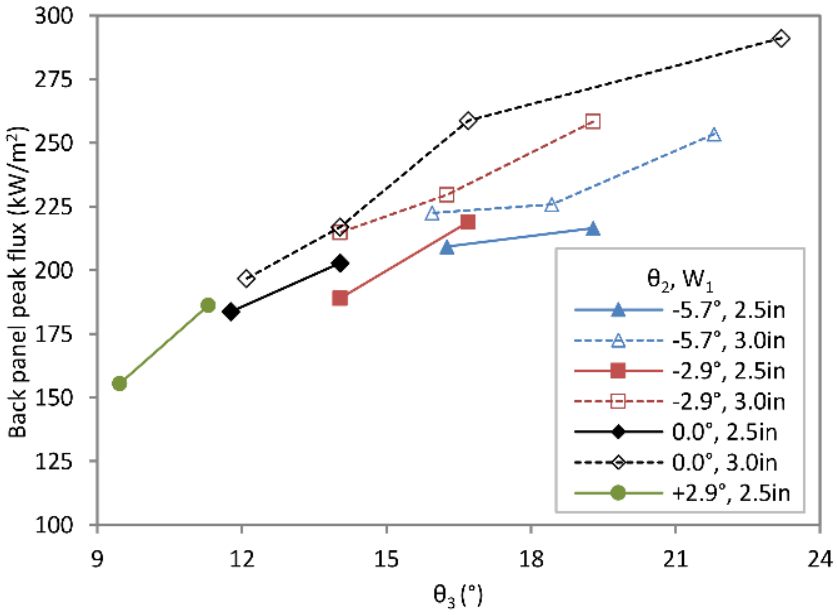

Figure 7. Back-panel (Panel 3) peak flux with respect to the geometry parameters.

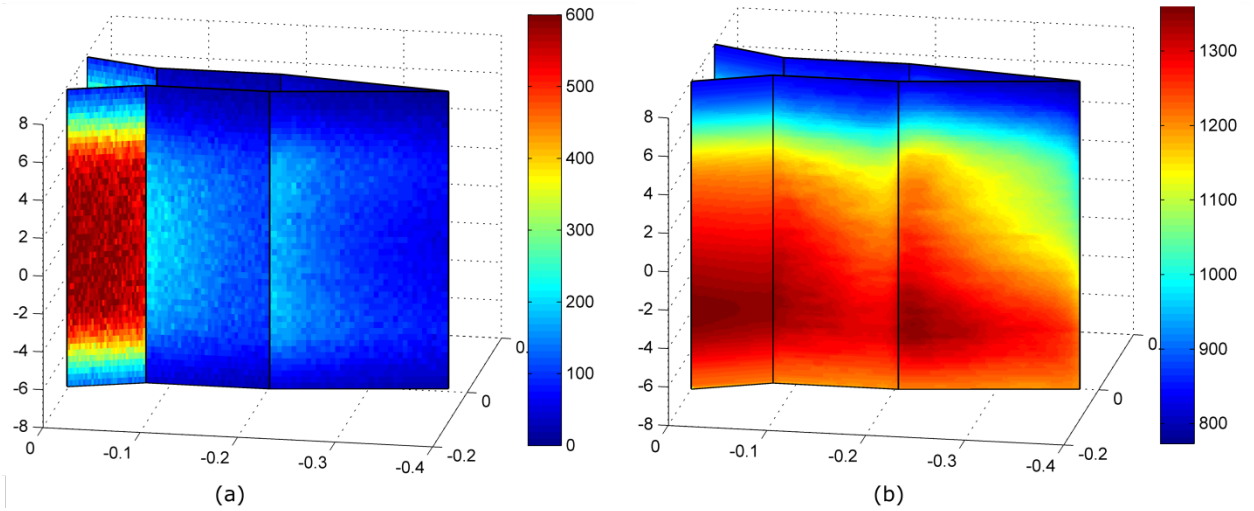

Figure 8. Simulated flux profile and temperature distribution for the panel wall of the north-facing cavity: (a) Absorbed flux profiles (kW/m^2) for Geometry 1, (b) Cavity wall temperature profile (K) from CFD simulation with base parameters

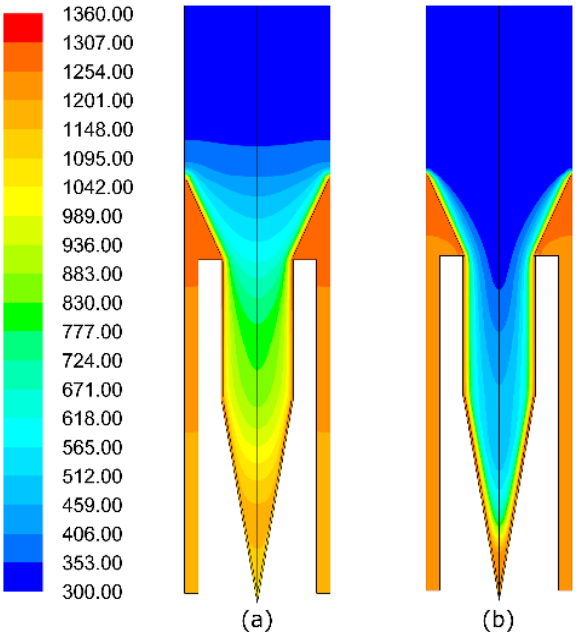

Figure 9. Temperature profiles (K) with base-case input parameters at (a) midpoint of receiver height, (b) 1 m above the bottom of receiver.

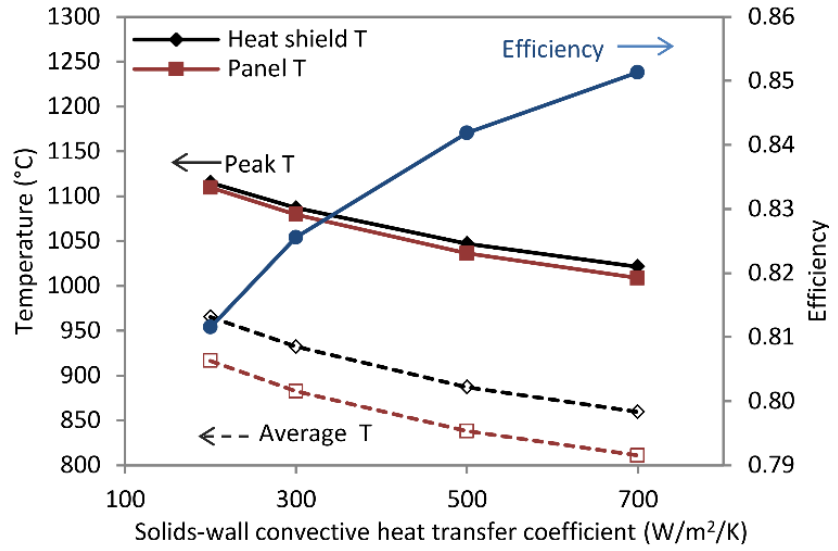

(a) $T_{s,in}$ = 500°C, $T_{s,out}$ = 900°C

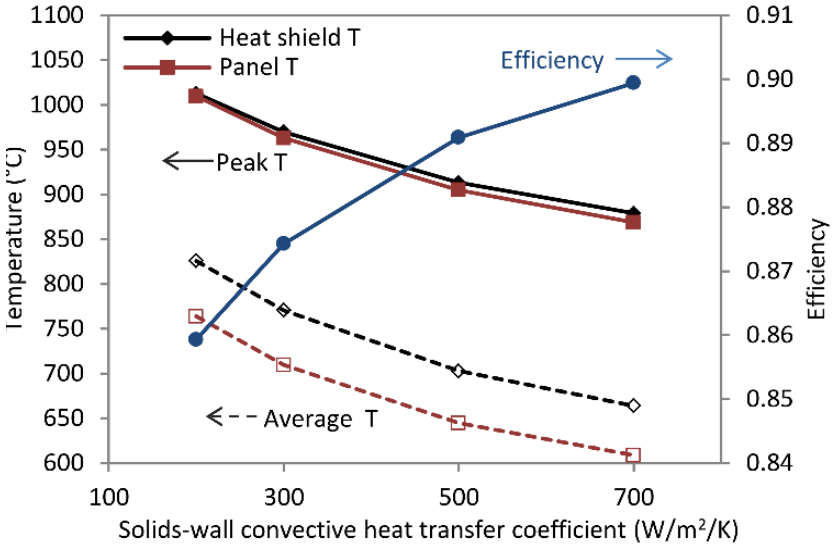

(b) $T_{s,in}$ = 200°C, $T_{s,out}$ = 750°C.

Figure 10. Sensitivity of north-facing cavity temperature and efficiency to effective solids-wall convective heat-transfer coefficients.

Table 1. Base-case simulation parameters

Parameter	Value (Geom. 1)	Value (Geom. 2)	Parameter	Value
H	16 m	16 m	Solids T_{in}	773 K (500°C)
W_1	0.0635 m	0.0635 m	Solids T_{out}	1,173 K (900°C)
W_2	0.0635 m	0.0635 m	h_{conv}	300 W/m^2·K
D_1	0.0762 m	0.0762 m	ρ_{wall} (solar)	0.1
D_2	0.127 m	0.127 m	α_{wall}, ε_{wall}	0.9
D_3	0.178 m	0.178 m	ε_{solids}	0.7
t_{wall}	0.0016 m	0.0016 m	Panel wall material	Haynes 230
θ_1	25°	20°	Heat pipe k_{eff}	5000 W/m·K
W_p	0.0254 m	0.0254 m		

Table 2. Base-case north-facing cavity performance

	$\theta_1 = 25°$		$\theta_1 = 20°$	
Avg. aperture q_{inc} (kW/m^2)	**1,055**		**1,055**	
Avg. panel q_{abs} (kW/m^2)	100		100	
Peak panel q_{abs} (kW/m^2)	235		220	
Avg. shield q_{abs} (kW/m^2)	445		380	
Solar reflection loss	4.0%		3.6%	
Solids inlet/outlet T (°C)	500 / 900	200 / 750	500 / 900	200 / 750
Peak heat-pipe T (°C)	1,087	970	1,056	933
Peak panel T (°C)	1,080	963	1,081	966
Infrared rad. loss	11.3%	6.9%	10.5%	6.3%
Convection loss	2.1%	1.6%	2.3%	1.8%
$\eta_{thermal}$	82.6%	87.4%	83.5%	88.4%